nanomaterials

MDPI

Article

Dependence of Positive Bias Stress Instability on Threshold Voltage and Its Origin in Solution-Processed Aluminum-Doped Indium Oxide Thin-Film Transistors

Jeong-Hyeon Na, Jun-Hyeong Park, Won Park, Junhao Feng, Jun-Su Eun, Jinuk Lee, Sin-Hyung Lee, Jaewon Jang, In Man Kang, Do-Kyung Kim *,† and Jin-Hyuk Bae *

School of Electronic and Electrical Engineering, Kyungpook National University, 80 Daehakro, Bukgu, Daegu 41566, Republic of Korea; jh2jh3@naver.com (J.-H.N.); jeef12345@naver.com (J.-H.P.); qkrdnjs0320@naver.com (W.P.); junhaosuhua@gmail.com (J.F.); wnstn0812@naver.com (J.-S.E.); kein98@knu.ac.kr (J.L.); sinhlee@knu.ac.kr (S.-H.L.); j1jang@knu.ac.kr (J.J.); imkang@ee.knu.ac.kr (I.M.K.)

* Correspondence: kdk7362@knu.ac.kr (D.-K.K.); jhbae@ee.knu.ac.kr (J.-H.B.)

† Current address: LG Display, Paju 10845, Republic of Korea.

Abstract: The initial electrical characteristics and bias stabilities of thin-film transistors (TFTs) are vital factors regarding the practical use of electronic devices. In this study, the dependence of positive bias stress (PBS) instability on an initial threshold voltage (V_{TH}) and its origin were analyzed by understanding the roles of slow and fast traps in solution-processed oxide TFTs. To control the initial V_{TH} of oxide TFTs, the indium oxide (InO_x) semiconductor was doped with aluminum (Al), which functioned as a carrier suppressor. The concentration of oxygen vacancies decreased as the Al doping concentration increased, causing a positive V_{TH} shift in the InO_x TFTs. The V_{TH} shift (ΔV_{TH}) caused by PBS increased exponentially when V_{TH} was increased, and a distinct tendency was observed as the gate bias stress increased due to a high vertical electric field in the oxide dielectric. In addition, the recovery behavior was analyzed to reveal the influence of fast and slow traps on ΔV_{TH} by PBS. Results revealed that the effect of the slow trap increased as the V_{TH} moved in the positive direction; this occured because the main electron trap location moved away from the interface as the Fermi level approached the conduction band minimum. Understanding the correlation between V_{TH} and PBS instability can contribute to optimizing the fabrication of oxide TFT-based circuits for electronic applications.

Keywords: oxide semiconductor; thin-film transistors (TFTs); bias instability; threshold voltage dependency; degradation mechanism

Citation: Na, J.-H.; Park, J.-H.; Park, W.; Feng, J.; Eun, J.-S.; Lee, J.; Lee, S.-H.; Jang, J.; Kang, I.M.; Kim, D.-K.; et al. Dependence of Positive Bias Stress Instability on Threshold Voltage and Its Origin in Solution-Processed Aluminum-Doped Indium Oxide Thin-Film Transistors. *Nanomaterials* **2024**, *14*, 466. https://doi.org/10.3390/nano14050466

Academic Editor: Antonino Gulino

Received: 5 January 2024
Revised: 4 February 2024
Accepted: 4 February 2024
Published: 4 March 2024

1. Introduction

Oxide thin-film transistors (TFTs) have been considered to be the building blocks for various next-generation electronic devices owing to their advantages, such as low processing temperature, high mobility, device-to-device uniformity, optical transparency, and high mechanical flexibility [1–3]. Large-area organic light-emitting diode (OLED) displays with indium–gallium–zinc-oxide TFTs have been commercialized [4,5]. Recently, the use of oxide TFTs in displays and monolithic three-dimensional integration has been actively studied [6]. The commercial feasibility of TFTs depends on their initial electrical characteristics. Among the various electrical parameters, such as mobility, subthreshold swing (SS), on/off current ratio ($I_{on/off}$), and threshold voltage (V_{TH}), V_{TH} is vital because it determines the depletion or enhancement mode of TFTs. Depletion- and enhancement-mode TFTs should be appropriately selected based on the product's characteristics [7,8]. In addition, V_{TH} should be effectively controlled to greater or less than 0. For example, when configuring a compensation circuit within a pixel in a display, the compensation error may increase if V_{TH} is too high or low [9,10]. In addition, a positive V_{TH} is required to

reduce circuit design complexity, as well as power consumption, when it is used as a gate driver circuit [11,12]. Thus, V_{TH} is an important initial parameter and should be effectively controlled during fabrication.

Based on their commercial usage, the robustness of TFT devices and their temperature, light, humidity, and bias stabilities must be ensured. Various external stresses, such as light or humidity, can be partially blocked by appropriately designing the device's structure, as well as introducing additional layers [13,14]. However, blocking the bias stress in TFTs is difficult as the electrical bias applied to drive the transistors is an internal stress. Therefore, the origin of bias stability must be studied to determine the robustness of the device. Extreme V_{TH} shifts and SS degradation occurs when negative gate bias and illumination stress are simultaneously applied [15–17]. When the oxide TFTs act as a switch rather than the current supplier to the OLEDs in displays, negative bias illumination stress (NBIS) is critical because the switching TFTs are typically turned off by negative gate bias [18]. However, the NBIS can be improved through the reduction of oxygen vacancies or peroxides, or introducing light-blocking metals [19]. Recently, oxide TFTs have been used in OLED displays [20], and positive bias stress (PBS) is becoming increasingly important because it is applied to the driving transistor that supplies a current to the OLED and gate driver circuit [18]. Although initial V_{TH} and PBS must be simultaneously considered, their correlation is not entirely clear. The PBS stability can be further improved based upon the initial V_{TH}. Moreover, solution-processed oxide TFTs have been actively studied owing to their advantages of high scalability and throughput [21–23]. However, they have poorer electrical stabilities than those fabricated by conventional sputtering because of the high density of physical and chemical defects that are generated during fabrication [24,25]. Therefore, the relation between V_{TH} and PBS stability must be further deduced. Additionally, VTH must be decreased in solution-processed oxide TFTs with relatively poor PBS stability than the sputtered oxide TFTs.

In this study, the correlation between an initial V_{TH} and PBS instability in solution-processed oxide TFTs was investigated. The degradation mechanism of PBS based on V_{TH} was demonstrated through the observation of the recovery behavior of oxide TFTs after PBS. Various molarities of Al were doped in the InO_x semiconductor to examine the dependency of V_{TH} on PBS instability; V_{TH} was successfully controlled in a wide range. The V_{TH} shift of Al-doped oxide TFTs was determined via the chemical and optical analysis of InO_x and indium-aluminum-oxide ($InAlO_x$) thin-film characteristics. Through measuring the PBS and the recovery of oxide TFTs, it was found that the initial V_{TH} and ΔV_{TH} induced by PBS have an exponential relation, regardless of the gate bias stress ($V_{G,stress}$). Moreover, analysis of the recovery behavior revealed that the role of slow traps in ΔV_{TH} became dominant in oxide TFTs with positive V_{TH}.

2. Materials and Methods

2.1. Preparation of Oxide Precursor Solutions

InO_x and $InAlO_x$ precursor solutions were prepared for fabricating oxide semiconductor thin films. A 0.1 M InO_x precursor solution was prepared by dissolving $In(NO_3)_3 \cdot xH_2O$ (Sigma-Aldrich, St. Louis, MO, USA) in 2-methoxyethanol (2-ME), which is generally used as a solvent for oxide precursor solutions [26,27]. To control the initial V_{TH}, $InAlO_x$ precursor solutions were prepared by adding 0.005, 0.010, and 0.015 M $Al(NO_3)_3 \cdot 9H_2O$ (Sigma-Aldrich, St. Louis, MO, USA) to 0.1 M InO_x precursor solution. The molar ratio of Al/In of the three prepared solutions are 0.05, 0.10, and 0.15. All solutions were stirred at 50 °C for 12 h.

2.2. Fabrication of Devices

Si/SiO_2 wafer substrates were prepared for gates and gate dielectrics. Wafers were cleaned via sonication for 10 min each in acetone, isopropyl alcohol, and deionized water. Then, the substrates were dried in an N_2 atmosphere, and annealed at 300 °C for 5 min to remove any residual moisture. The water etchant–based photo patterning method was

used to deposit the patterned oxide semiconductor for the fabrication of high-performance oxide TFTs [28]. Figure 1a schematizes the fabrication process of InO_x and $InAlO_x$ thin films. The precursor solutions were spin-coated at 3000 rpm for 20 s onto a cleaned Si/SiO_2 wafer (Step 1). The precursor solution-deposited wafer was soft baked at 100 °C for 30 s (Step 2). Then, a fine metal mask was placed on the wafer to irradiate ultraviolet (UV) light in a selective area. The UV was exposed to InO_x for 120s and $InAlO_x$ for 150 s under an N_2 atmosphere (Step 3). UV irradiation (25 mW cm^{-2}) was conducted via a low-pressure mercury lamp with two main wavelengths, namely 253.7 (90%) and 184.9 nm (10%). UV photons induced the decomposition of nitrate ligand via photochemical cleavage. Then, the wafer was etched in a deionized water etchant for 1 min (Step 4). Patterned InO_x and $InAlO_x$ were annealed at 100 °C for 10 min and 270 °C for 2 h, respectively, on a hot plate in the air (Step 5). In this series of processes, hydrolysis and condensation reactions were promoted, which yielded low-defect high-quality oxide thin films. Lastly, a 50-nm-thick Al film was deposited for source and drain electrodes using thermal evaporation (Step 6). The channel length (L) and width (W) were 100 and 1000 µm, respectively. The patterned thin films or TFTs fabricated using InO_x, $InAlO_x$ with 0.005 M Al doping, $InAlO_x$ with 0.010 M Al doping, and $InAlO_x$ with 0.015 M Al doping were named InO_x, $InAlO_x$-1, $InAlO_x$-2, and $InAlO_x$-3, respectively, as shown in Figure 1b.

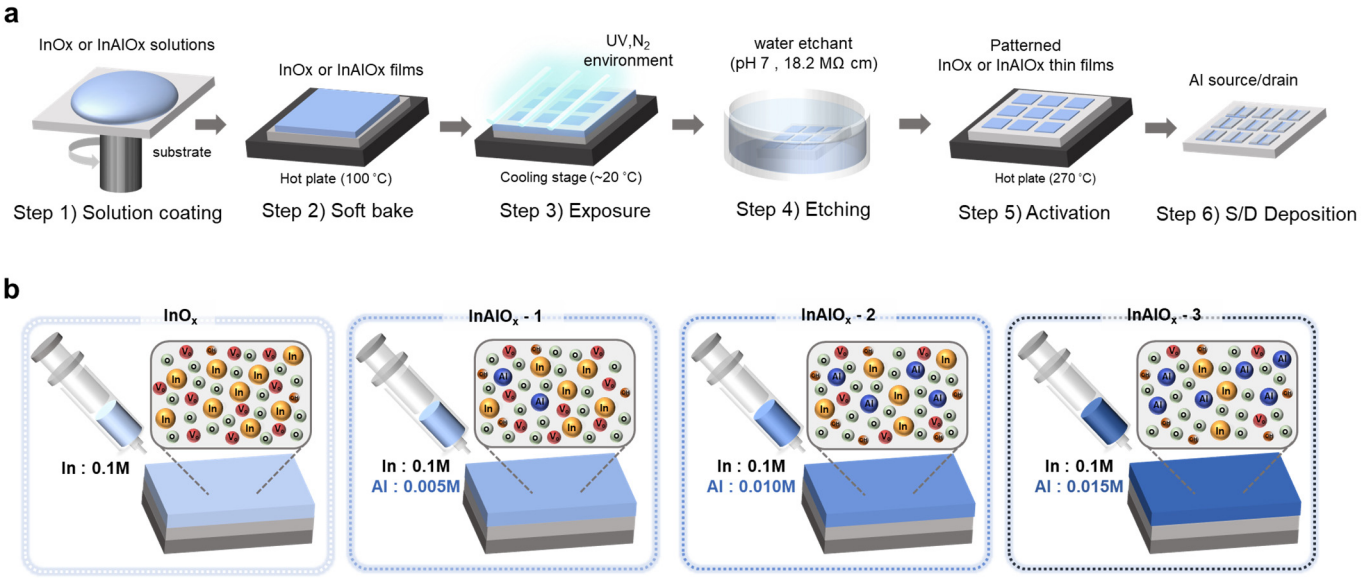

Figure 1. (**a**) Schematic of the device fabrication process. (**b**) Schematic of the $InAlO_x$ thin films with various Al doping concentration.

2.3. Analysis of Thin Films and Devices

Chemical compositions of InO_x and $InAlO_x$ thin films were investigated using X-ray photoelectron spectroscopy (XPS; ThermoFisher Scientific, NEXSA, Waltham, MA, USA) with an Al Kα (1486.6 eV) light source. To determine the optical properties, such as the bandgap, of the deposited oxide semiconductor films, a UV–visible (UV–Vis) spectrophotometer (Perkin Elmer, Waltham, MA, USA, LAMBDA 265) was used. The InO_x and $InAlO_x$ films deposited on cleaned glass were measured by a transmittance mode. A probe station (MS Tech, Oak Ridge, TN, USA, MST-6VC) was used to measure the transfer curves of InO_x TFTs under temperature variations. The electrical characteristics of the devices were obtained using a semiconductor parameter analyzer (4200-SCS, Keithley, Cleveland, OH, USA) combined with an ultrafast I–V module (4225-PMU, Keithley). All devices were measured at room temperature in a dark environment.

3. Results

InO_x and $InAlO_x$ thin films with various molarities were fabricated to demonstrate their electrical characteristics, as shown in Figure 1a. The changes in the atomic structure with increasing Al doping concentration were evaluated via XPS analysis. Figure 2a shows the O1s spectra of InO_x, $InAlO_x$-1, $InAlO_x$-2, and $InAlO_x$-3. The oxygen bonding states were analyzed via deconvolution into three Gaussian Lorentzian peaks corresponding to the oxygen species of the metal–oxide (M–O), oxygen vacancy (V_o), and metal–hydroxide (M-OH) centered at ~529.6, ~531.0, and ~531.8 eV, respectively [29–31]. The oxygen-binding energy of Al was higher than that of In; therefore, Al suppressed the oxygen defects in the active layer [32]. As shown in Figure 2b, as the Al doping concentration increases, M–O bonding increases and V_o decreases, thereby increasing the carrier concentration [33]. The M–OH bonding increases with the Al doping concentration, which is explained via the M–OH condensation reaction. At a certain temperature, two M–OH bonds form an M–O–M bond via condensation; however, the reaction does not progress when Al is doped. Figure 2c shows the binding energy of the element extracted from XPS. As the Al doping concentration increases, the Al2p peak can be clearly observed. In step 2 (Figure 1a), a large amount of nitrate ligands in the oxide film disappears; in step 3 (Figure 1a), the nitrate ligands inside the film are decomposed by UV irradiation, hydroxyl radical species, and M−OH bond formation [28]. Therefore, the N1s peak was not clear for all the TFT devices. The C–O/C–OH bond with a binding energy of ~287.0 eV was decomposed via UV irradiation, and only the C–H/C–C bond with a binding energy of ~285.0 eV remained; all TFT devices showed the same c1s peak [34].

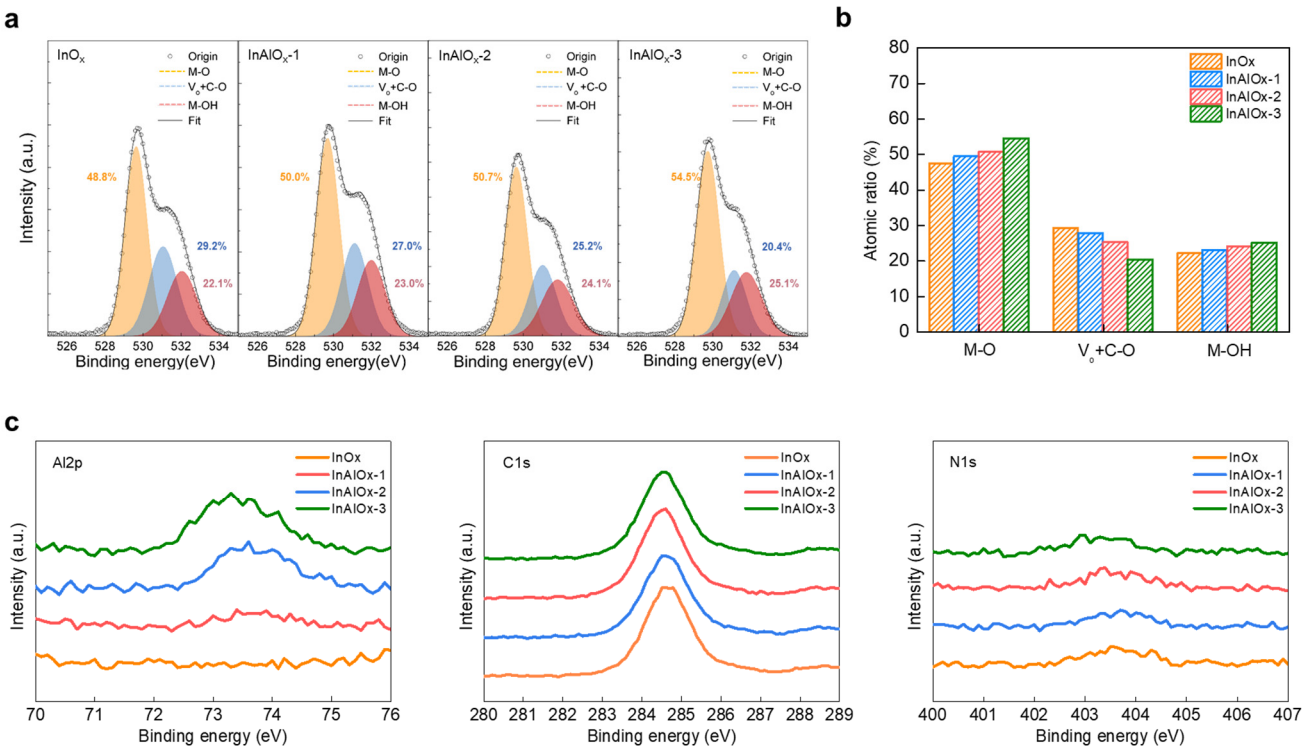

Figure 2. (**a**) XPS O 1s spectra for InO_x and $InAlO_x$ semiconductors with various Al doping concentrations. (**b**) The comparison of the atomic percentages of M–O, Vo + C–O, and M–OH of $InAlO_x$ semiconductors with various Al doping concentrations. (**c**) XPS Al 2p, C 1s, and N 1s spectra for InO_x and $InAlO_x$ semiconductors with various Al doping concentrations.

To understand the charge transport mechanism, the interfacial energy-level alignments between the active layer and source/drain electrode must be elucidated. The energy band alignment of InO_x and $InAlO_x$ thin films was investigated via UV–Vis spectrophotometry and XPS analysis. The optical bandgap (E_g) was obtained from the extrapolated linear

fit of $(\alpha h\nu)^2$ versus the photon energy, as shown in Figure 3a. The extracted E_g values of InO_x, $InAlO_x$-1, $InAlO_x$-2, and $InAlO_x$-3 were 3.72, 3.80, 3.81, and 3.86 eV, respectively. The atomic radius of In was 156 pm, larger than that of Al. Thus, the substitution of a smaller atom (Al) in the composition with a larger atom (In) decreases the E_g; these results coincide with the theoretical expectations [35]. As shown in Figure 3b, as the Al doping concentration increases, the valence band offset decreases from 2.58 to 2.11. Thus, with increasing Al doping concentration, E_g increases and valence band offset decreases, thereby increasing the conduction band offset (Figure 3c). This result suggests that as the Al doping concentration increases, V_o and carrier concentration decrease [36,37].

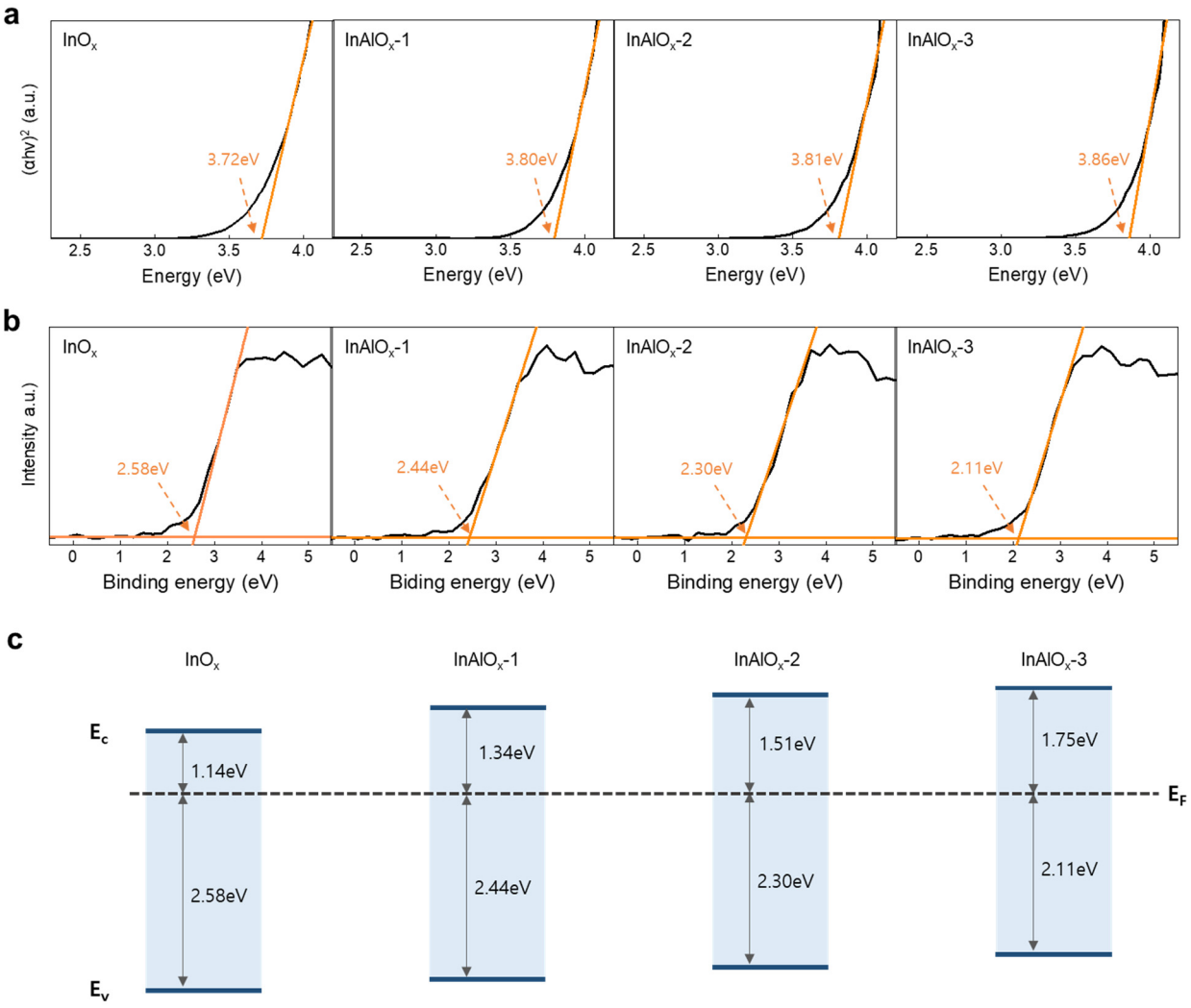

Figure 3. (**a**) Optical bandgap and (**b**) valence band offset spectra for InO_x and $InAlO_x$ semiconductors with various Al doping concentrations. (**c**) Energy band alignment of InO_x and $InAlO_x$ semiconductors with various Al doping concentrations.

To demonstrate the electrical characteristics based on the carrier concentration of the oxide semiconductor, TFTs containing InO_x, $InAlO_x$-1, $InAlO_x$-2, and $InAlO_x$-3 with a bottom-gate, top-contact structure were fabricated. Figure 4a shows the transfer characteristics of InO_x, $InAlO_x$-1, $InAlO_x$-2, and $InAlO_x$-3. Gate voltage (V_G) swept from −20 to 30 V with a 0.5 V step, and drain voltage (V_D) was fixed at 30 V. The gray line shows the gate leakage current (I_G). As shown in the transfer curves, all TFTs had acceptable switching characteristics with low off current levels of 10^{-12}–10^{-11} A, regardless of the doping concentration. In contrast, the curves positively shifted, and on current gradually decreased as the Al doping concentration increased, which originated from the decrease in

the carrier concentration of semiconductors as the Al doping concentration increased. For a more detailed comparison, the summarized results of the electrical parameters of InO_x and $InAlO_x$ TFTs are shown in Figure 4b. Here, V_{TH} was defined as the value of V_G that induces drain current (I_D) = 10 nA × W/L at V_D = 30 V. A positive shift of V_{TH}, increase in SS, and decrease in field-effect mobility in saturation region (μ_{FE}) was observed. A positive shift of V_{TH} and a decrease in μ_{FE} are reasonable because the Al doping suppresses the formation of V_o, thereby decreasing the carrier concentration, as confirmed by the XPS results. In addition, the maximum trap density ($N_{T,max}$) increased with Al doping concentration due to an increase in the SS based on the following equation:

$$SS = \frac{qk_B\,T(N_T t_{ch} + D_{it})}{C_{ox}\log(e)}, \quad (1)$$

where k, q, T, and C_i are the Boltzmann constant, elementary electron charge, and absolute temperature, respectively. N_T and D_{it} are the number of fast bulk traps and semiconductor-insulator interfacial traps. $N_{T,max}$ of InO_x, $InAlO_x$-1, $InAlO_x$-2, and $InAlO_x$-3 are 4.66, 6.11, 6.96, 7.96 × 10^{18} cm^{-3} eV^{-1}, respectively.

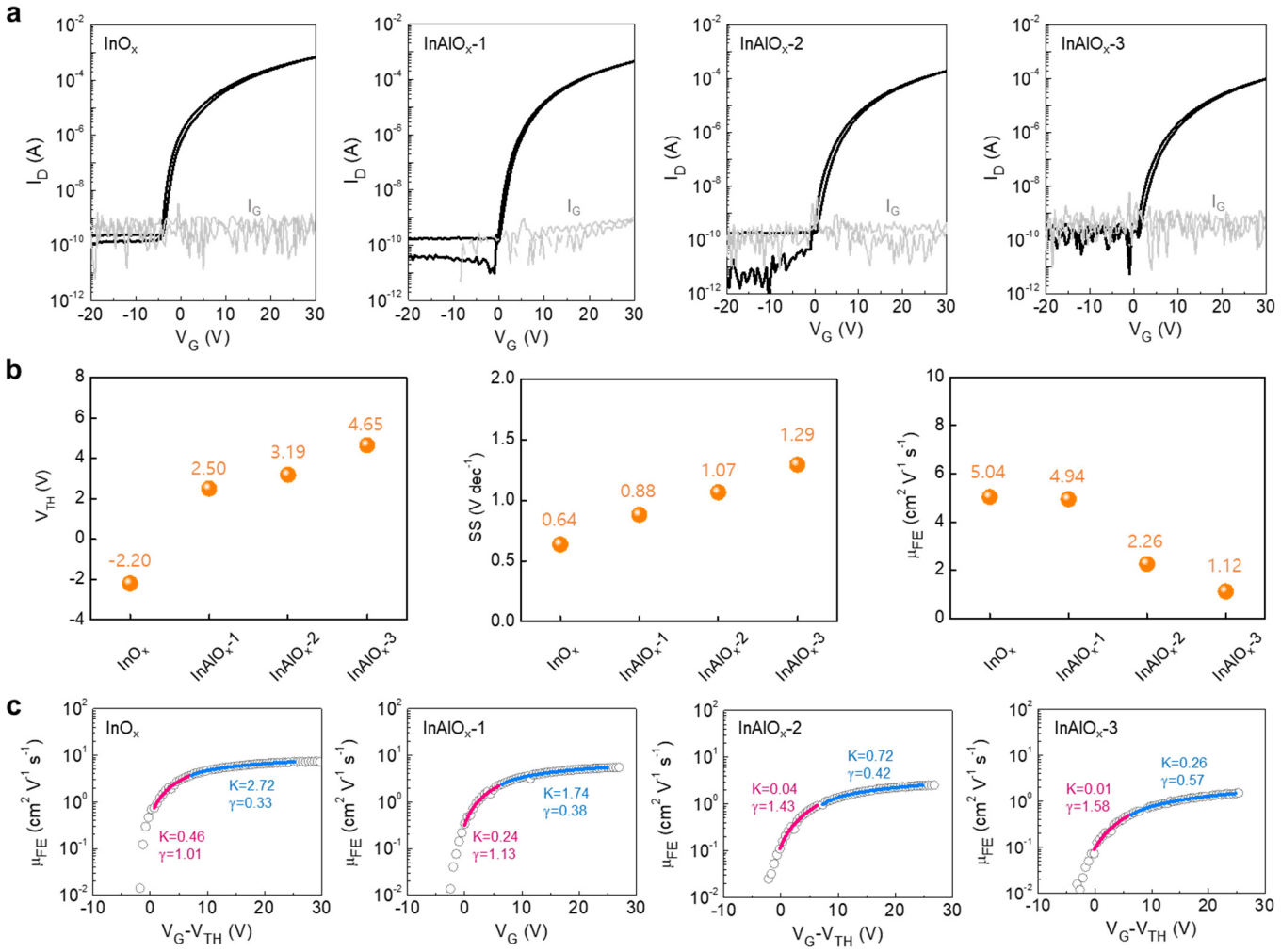

Figure 4. (**a**) Transfer characteristics of $InAlO_x$ TFTs with various Al doping concentrations. (**b**) Electrical parameters including threshold voltage, subthreshold swing, and field-effect mobility of $InAlO_x$ TFTs with various Al doping concentrations. (**c**) Field-effect mobility versus overdrive voltage of $InAlO_x$ TFTs with various Al doping concentrations.

Unlike single-crystal Si-based transistors that follow the band transport theory, oxide semiconductor–based transistors have a different charge transport mechanism due to their atomic structural disorder. In general, the current–voltage behavior of oxide TFTs is modeled based on trap-limited conduction (TLC) and percolation [38,39]. In particular, the charge transport mechanism varies based on the electron concentration in the semiconductor, which is identified through the power-law dependence of mobility [40]. Here, a power-law equation was employed in the (V_G-V_{TH})—μ_{FE} curve to investigate the influence of Al doping on carrier trapping and thermal release at the tail states and percolation in the above-threshold regime in oxide TFTs, as shown in Figure 4c.

$$\mu_{FE} = K(V_G - V_{T,P})^{\gamma}, \quad (2)$$

where V_P is the percolation voltage, and K and γ are related to the nature of the electron transport. In a typical power-law model, TLC affects the constant K, and percolation conduction determines the exponent γ [41]. To observe the transition of the electron conduction mechanism by V_G, each curve was fitted in the low V_G and high V_G regions by the power-law equation. In low V_G region, the K values of InO_x, $InAlO_x$-1, $InAlO_x$-2, and $InAlO_x$-3 are 0.46, 0.24, 0.04, and 0.01, respectively. This suggests that the TLC prevails as the initial V_{TH} positively shifts in the oxide TFTs. As V_{TH} shifts positively in the low V_G region, γ also tends to increase, suggesting that electron conduction is greatly restricted by the potential barrier. Meanwhile, in high V_G region, K and γ values according to Initial V_{TH} show the same tendency as those in the low V_G region. Interestingly, K and γ overall show higher and lower values, respectively, compared to the low V_G region. This implies that charge transport by percolation is dominant rather than the tail states as the V_G increase.

The PBS stability, along with the initial characteristics of the device, should be considered for the practical use of the device. Then, to verify the influence of Al doping concentration on the PBS-induced instability, V_{TH} characteristics were determined based on the PBS and recovery. Figure 5 shows the time evolution of V_{TH} shift (ΔV_{TH}) during PBS and subsequent recovery. For PBS, a $V_{G,stress}$ of 10 or 30 V was applied for 1000 s. To avoid TFT degradation and asymmetric charge trapping due to current stress, a V_D of 0 V was applied during stress. Immediately after 1000 s of PBS, recovery was followed for 2000 s at V_G = 0 V and V_D = 0 V. As shown in Figure 5a, V_{TH} shifted positively during PBS with a $V_{G,stress}$ of 10 V, and the degree of recovery tended to increase with Al doping concentration. V_{TH} recovers rapidly in the early stages of recovery after stress and then tends to saturate [42,43]. InO_x TFTs recovered at the fastest rates, and after recovery for 2000 s, V_{TH} returned close to its initial state. $InAlO_x$-3 with a high Al doping concentration showed the slowest recovery speed and a high ΔV_{TH}, even after recovery at 2000 s. This characteristic means that some of the electrons trapped in the interface and gate dielectric by PBS are easily detrapped by the recovery phase, but the rest remain without being detrapped. Moreover, the results show that these trap/detrap characteristics differ depending on the Al doping concentration.

The stretched-exponential time dependence of ΔV_{TH} suggests that ΔV_{TH} originated from electron trapping at the trap sites [43,44]. The stretched-exponential equation for ΔV_{TH}(t) is as follows:

$$\Delta V_{TH}(t) = \Delta V_{TH0}\{1 - exp[-(t/\tau)^{\beta}]\}, \quad (3)$$

where ΔV_{TH0} is the ΔV_{TH} at infinite time, β is the stretched-exponential exponent, and τ is the characteristic trapping time of carriers. ΔV_{TH} by PBS with a $V_{G,stress}$ of 10 V for InO_x and $InAlO_x$ TFTs were fitted to the stretched-exponential equation, and β and τ for each device were extracted, as shown in Figure 5b. τ decreased as the Al doping concentration increased, implying that electrons were easily trapped in the trap site. Figure 5c,d show the time evolution of ΔV_{TH} by PBS with a $V_{G,stress}$ of 30 V and subsequent recovery, and the corresponding β and τ during PBS, respectively. ΔV_{TH} at a $V_{G,stress}$ of 30 V shows a similar trend to the PBS with $V_{G,stress}$ = 10 V, as shown in Figure 5a,b. Notably, as $V_{G,stress}$

increases, ΔV_{TH} becomes larger in the same device and the correlation between Al doping concentration and ΔV_{TH} becomes clearer. Through a quantitative comparison of τ, it is confirmed that charge trapping occurs more effectively with strong vertical electric field as $V_{G,stress}$ increases.

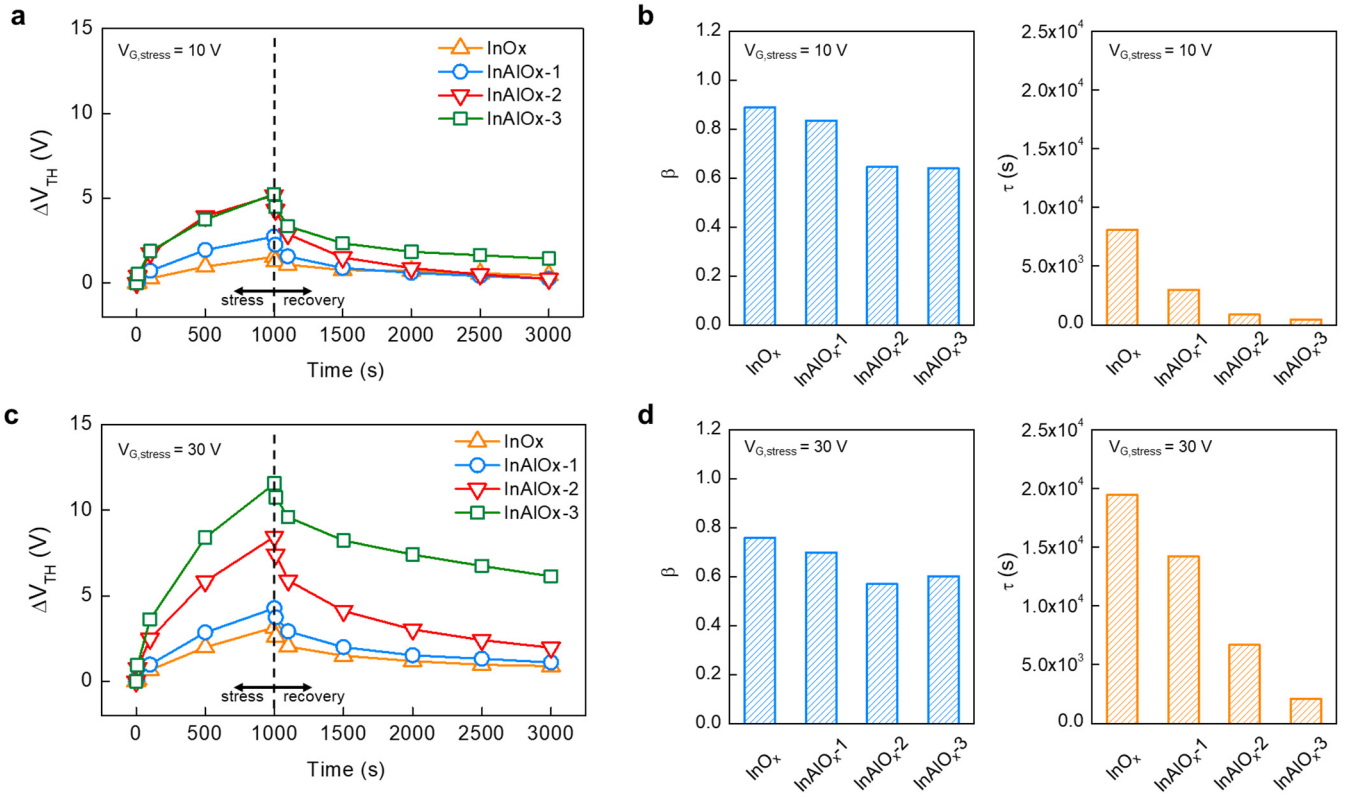

Figure 5. (**a**) Time evolution of ΔV_{TH} during the low V_G stress (V_G = 10 V, V_D = 0 V, t = 1000 s) and subsequent recovery (V_G = 0 V, V_D = 0 V, t = 2000 s) phases, and (**b**) corresponding stretched exponential function parameters of InAlOx TFTs with various Al doping concentrations. (**c**) Time evolution of ΔV_{TH} during the high V_G stress (V_{GS} = 30 V, V_{DS} = 0 V, t = 1000 s) and subsequent recovery (V_{GS} = 0 V, V_{DS} = 0 V, t = 2000 s) phases and (**d**) corresponding stretched-exponential function parameters of $InAlO_x$ TFTs with various Al doping concentrations.

Based on the initial electrical characteristics according to the Al doping concentration in InO_x TFTs, the influence of initial V_{TH} on ΔV_{TH} is further revealed. Figure 6a depicts the time evolution of ΔV_{TH}. Al-doped InO_x TFTs show higher ΔV_{TH} as V_{TH} shifts more positively, or as $V_{G,stress}$ increases (Figure 5). Here, electrons that are not easily detrapped during the recovery phase are considered as slow traps, whereas those that are detrapped during the recovery phase are treated as fast traps [42]. Variations in ΔV_{TH} based on V_{TH} were plotted by increasing the number of measured samples to clearly identify the correlation between V_{TH} and ΔV_{TH}, as shown in Figure 6b. Regardless of $V_{G,stress}$, ΔV_{TH} tended to increase exponentially as V_{TH} increased. The ΔV_{TH} by PBS with 10 and 30 V for devices with a V_{TH} in the range of −2–4 V was fitted with an exponential function, and showed high R^2 values of 0.88 and 0.93, respectively. As $V_{G,stress}$ increased from 10 to 30 V, the trend became clear. $\Delta V_{TH,slow}$ was extracted from the recovery behavior, and the ratio of slow trap according to V_{TH} is shown in Figure 6c. In enhancement-mode TFTs with a V_{TH} of 0 V or higher, $\Delta V_{TH,slow}/\Delta V_{TH}$ tended to increase exponentially as V_{TH} increased, whereas in depletion-mode TFTs, an opposite trend was confirmed. This trend could be fitted with a parabola function and showed high R^2 values of 0.66 and 0.81 when $V_{G,stress}$ was 10 and 30 V, respectively. PBS with a $V_{G,stress}$ of 30 V had a higher slow trap rate than when that with a $V_{G,stress}$ of 10 V.

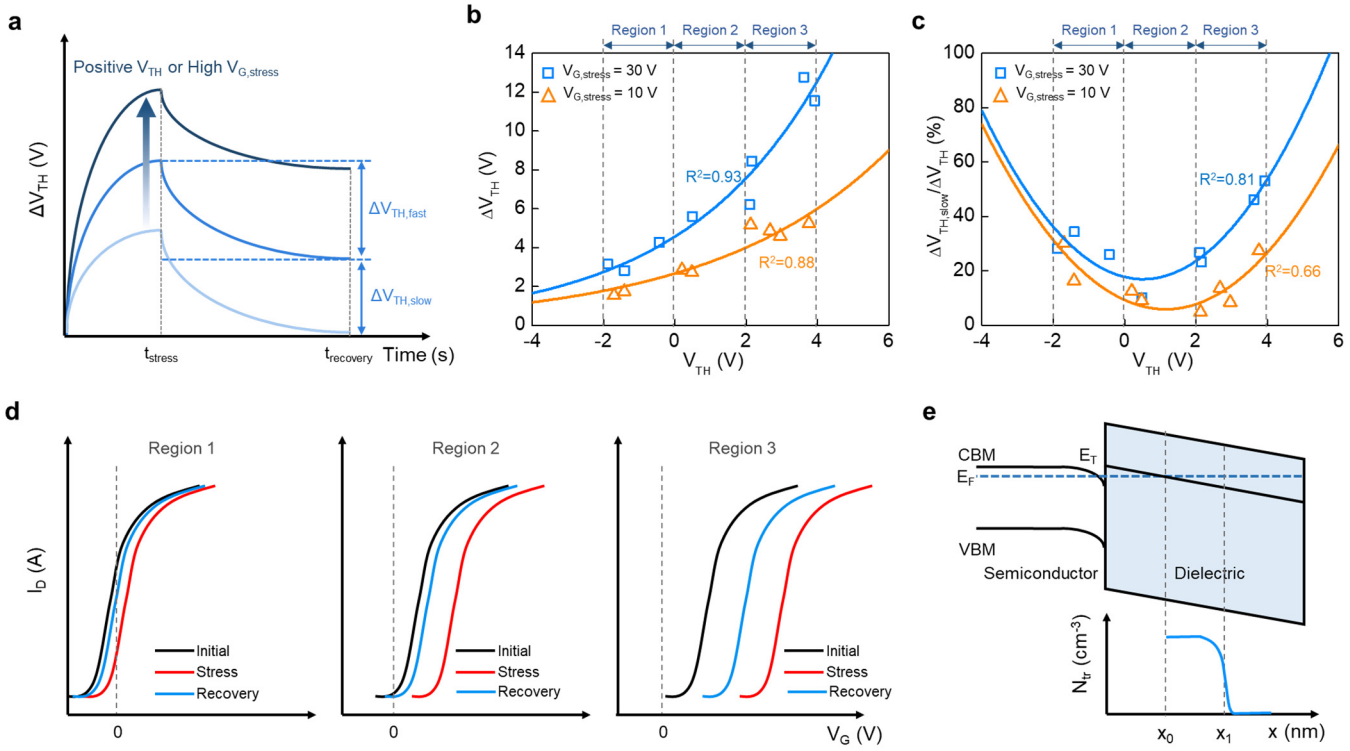

Figure 6. Dependence of (**a**) time evolution of ΔV_{TH} and corresponding slow trapping ($\Delta V_{TH,slow}$) and fast trapping ($\Delta V_{TH,fast}$) components. (**b**) ΔV_{TH} and (**c**) $\Delta V_{TH,slow}/\Delta V_{TH}$ on the initial V_{TH} of oxide TFTs. Two devices each from InO_x, $InAlO_x$-1, $InAlO_x$-2, and $InAlO_x$-3 were measured. (**d**) Schematic of transfer characteristics at initial state, after stress, and after recovery of oxide TFTs in regions 1, 2, and 3. (**e**) The energy band of oxide TFTs and extracted trapped electron distribution in the fast and deep gate dielectric traps.

To estimate the charge transport mechanism, we divided the plot of ΔV_{TH} against V_{TH} into three regions, with V_{TH} of −2–0 V, 0–2 V, and 2–4 V named as regions 1, 2, and 3, respectively (Figure 6a,b). Figure 6d illustrates the transfer characteristics at the initial state, after stress, and after recovery by region. From Region 1 to 3, the initial V_{TH} shifts positively and shows a large ΔV_{TH} after stress. This ΔV_{TH} dependence on V_{TH} can be explained based on the band diagram, where x_0 is the intersection of the Fermi level (E_F) and trap level (E_T), and most electrons are trapped between x_0 and x_1, as shown in Figure 6e [45,46]. As shown in Figure 3c, as the Al doping concentration increases, E_F approaches the conduction band minimum. Thus, x_1, where the injected charge is mainly located, moves away from the interface based on the function of the electron transfer distance [45]. In other words, electrons trapped deep cannot be easily detrapped through recovery at room temperature, and as V_{TH} shifts positively, the rate of slow trap increases. Meanwhile, ΔV_{TH} increases with V_G and stress caused by x_1 moving away from the semiconductor–dielectric interface as the electric field applied to the oxide dielectric increases, implying that the electrons are trapped deeper [46]. Notably, compared to ΔV_{TH}, the degree of recovery in region 1 was less than that in region 2. This is because depletion-mode TFTs do not form a flat band at V_G = 0 V, but still form charge accumulation by band bending, forming x_0. In addition, region 2 showed smaller ΔV_{TH} and higher recovery characteristics compared to region 3. These results suggest that as the initial V_{TH} increases or the carrier concentration of the semiconductor decreases, the influence of the slow trap on PBS degradation increases. Thus, an inappropriate positive V_{TH} may considerably deteriorate the short- and long-term stabilities.

4. Conclusions

The linearity and resolution of the delay line has a great effect on transmitter performance. In order to overcome the bottleneck of low linearity and low resolution, an improved delay line structure is proposed with a calibration algorithm to conquer PVT variations for this all-digital design. Measurement results show that the proposed structure with the calibration algorithm can evidently improve the linearity and resolution of the delay line. In summary, we demonstrated the correlation between V_{TH} and ΔV_{TH} in solution-processed oxide TFTs. The oxygen vacancy and bandgap were controlled by tuning the Al doping concentration in the Al-doped InO_x, which changed the initial V_{TH} of the oxide TFTs. As V_{TH} increased, ΔV_{TH} due to PBS increased exponentially, and the deterioration became more severe as the $V_{G,stress}$ increased from 10 to 30 V. Using the stretched-exponential function, it was revealed that the positive V_{TH} and high $V_{G,stress}$ decreased the characteristic trapping time of carriers, implying that the charge trapping occurs effectively. Based on the recovery characteristics after PBS, the slow trap acts dominantly to ΔV_{TH}, and trapped electrons are not easily detrapped under a high $V_{G,stress}$ or in TFTs with a positive V_{TH}. In case of PBS with a $V_{G,stress}$ of 30 V, $\Delta V_{TH,slow}/\Delta V_{TH}$ showed a significant difference of 10.07% and 53.12% for TFTs with V_{TH} of 0.49 and 3.93 V, respectively. The results of this study can be used to determine the initial V_{TH} considering PBS and improving PBS in solution-processed oxide TFTs.

Author Contributions: Conceptualization, J.-H.N., D.-K.K. and J.-H.B.; methodology, J.-H.N., J.-H.P. and W.P.; validation, J.-H.N.; formal analysis, J.F., J.-S.E. and J.L.; investigation, D.-K.K. and J.-H.B.; resources, J.J. and I.M.K.; data curation, J.-H.N. and S.-H.L.; writing—original draft preparation, J.-H.N.; writing—review and editing, D.-K.K. and J.-H.B.; supervision, D.-K.K. and J.-H.B. All authors have read and agreed to the published version of the manuscript.

Funding: This work was supported by a National Research Foundation of Korea (NRF) grant funded by the Korea government (MSIT) (2021R1A2C1011429). This research was also supported by the MSIT (Ministry of Science and ICT), Korea under the Innovative Human Resource Development for Local Intellectualization support program (IITP-2024-RS-2022-00156389), as well as supervised by the IITP (Institute for Information and Communications Technology Planning and Evaluation).

Data Availability Statement: Data are contained within the article.

Conflicts of Interest: Author Do-Kyung Kim was employed by the company LG Display. The remaining authors declare that the research was conducted in the absence of any commercial or financial relationships that could be construed as a potential conflict of interest.

References

1. Fortunato, E.; Barquinha, P.; Martins, R. Oxide semiconductor thin-film transistors: A review of recent advances. *Adv. Mater.* **2012**, *24*, 2945–2986. [CrossRef]
2. Ma, L.-Y.; Soin, N.; Aidit, S.N.; Rezali, F.A.M.; Hatta, S.F.W.M. Recent advances in flexible solution-processed thin-film transistors for wearable electronics. *Mater. Sci. Semicond.* **2023**, *165*, 107658. [CrossRef]
3. Xu, W.; Li, H.; Xu, J.-B.; Wang, L. Recent advances of solution-processed metal oxide thin-film transistors. *ACS. Appl. Mater. Interfaces* **2018**, *10*, 25878–25901. [CrossRef]
4. Sheng, J.; Jeong, H.-J.; Han, K.-L.; Hong, T.; Park, J.-S. Review of recent advances in flexible oxide semiconductor thin-film transistors. *J. Inf. Disp.* **2017**, *18*, 159–172. [CrossRef]
5. Thomas, S.R.; Pattansattayavong, P.; Anthopoulos, T.D. Solution-processable metal oxide semiconductors for thin-film transistor applications. *Chem. Soc. Rev.* **2013**, *42*, 6910–6923. [CrossRef]
6. Zhang, J.; Wang, W.; Zhu, J.; Wang, J.; Zhao, C.; Zhu, T.; Ren, Q.; Liu, Q.; Qiu, R.; Zhang, M.; et al. Ultra-flexible monolithic 3d complementary metal-oxide-semiconductor electronics. *Adv. Funct. Mater.* **2023**, *33*, 3397–3398. [CrossRef]
7. Wang, M.; Liang, L.; Luo, H.; Zhang, S.; Zhang, H.; Javaid, K.; Cao, H. Threshold voltage tuning in a-IGZO tfts with ultrathin SnOx capping layer and application to depletion-load inverter. *IEEE Electron Device Lett.* **2016**, *37*, 422–425. [CrossRef]
8. Oh, J.; Jung, K.-M.; Jung, E.K.; Lee, J.; Lee, S.-Y.; Park, K. Novel Driving Methods of Gate Driver for Enhancement- and Depletion-Mode Oxide TFTs. *IEEE J. Electron Devices Soc.* **2020**, *8*, 67–73. [CrossRef]
9. Yi, S.; Huo, X.; Liao, C.; Wang, Y.; Wu, J.; Jiao, H.; Zhang, M.; Zhang, S. An a-IGZO TFT pixel circuit for amoled display systems with compensation for mobility and threshold voltage variations. In Proceedings of the 2018 IEEE International Conference on Electron Devices and Solid State Circuits (EDSSC), Shenzhen, China, 6–8 June 2018; pp. 1–2.

10. Bagheri, M.; Cheng, X.; Zhang, J.; Lee, S.; Ashtiani, S.; Nathan, A. Threshold voltage compensation error in voltage programmed amoled displays. *J. Disp. Technol.* **2016**, *12*, 658–664. [CrossRef]
11. Kim, J.-H.; Oh, J.; Park, K.; Kim, Y.-S. IGZO TFT gate driver circuit with large threshold voltage margin. *Displays* **2018**, *53*, 1–7. [CrossRef]
12. Choi, S.; Park, J.; Hwang, S.-H.; Kim, C.; Kim, Y.-S.; Oh, S.; Baeck, J.H.; Bae, J.U.; Noh, J.; Lee, S.-W.; et al. Excessive oxygen peroxide model-based analysis of positive-bias-stress and negative-bias-illumination-stress instabilities in self-aligned top-gate coplanar In–Ga–Zn–O thin-film transistors. *Adv. Mater.* **2022**, *8*, 2101062. [CrossRef]
13. Yu, E.S.; Kim, S.G.; Moon, S.J.; Bae, B.S. Improving the electrical stability of a-IGZO TFT through gate surround structures. *Electron. Lett.* **2023**, *59*, e12977. [CrossRef]
14. Park, J.S.; Maeng, W.-J.; Kim, H.-S.; Park, J.-S. Review of recent developments in amorphous oxide semiconductor thin-film transistor devices. *Thin Solid Films* **2012**, *520*, 1679–1693. [CrossRef]
15. Kim, W.-S.; Lee, Y.-H.; Cho, Y.-J.; Kim, D.-K.; Park, K.T.; Kim, O. Effect of wavelength and intensity of light on a-InGaZnO tfts under negative bias illumination stress. *ECS J. Solid State Sci. Technol.* **2016**, *6*, Q6–Q9. [CrossRef]
16. Li, Y.; Pei, Y.L.; Hu, R.Q.; Chen, Z.M.; Zhao, Y.; Shen, Z.; Fan, B.F.; Liang, J.; Wang, G. Effect of channel thickness on electrical performance of amorphous IGZO thin-film transistor with atomic layer deposited alumina oxide dielectric. *Curr. Appl. Phys.* **2014**, *14*, 941–945. [CrossRef]
17. Kim, Y.; Kim, C. Enhancement of electrical stability of metal oxide thin-film transistors against various stresses. *J. Mater. Chem.* **2023**, *11*, 7121–7143. [CrossRef]
18. Jeong, J.K. Photo-bias instability of metal oxide thin film transistors for advanced active matrix displays. *J. Mater. Res.* **2013**, *28*, 2071–2084. [CrossRef]
19. Kim, B.S.; Jeong, Y.T.; Lee, D.; Choi, T.Y.; Jung, S.-H.; Choi, J.W.; Yang, C.; Jo, K.; Lee, B.-J.; Park, E.; et al. Solution-processed zinc-indium-tin oxide thin-film transistors for flat-panel displays. *Appl. Phys. Lett.* **2013**, *103*, 072110. [CrossRef]
20. Mo, Y.G.; Kim, M.; Kang, C.K.; Jeong, J.H.; Park, Y.S.; Choi, C.G.; Kim, H.D.; Kim, S.S. Amorphous-oxide tft backplane for large-sized AMOLED TVs. *J. Soc. Inf. Disp.* **2011**, *19*, 16–20. [CrossRef]
21. Chen, R.; Lan, L. Solution-processed metal-oxide thin-film transistors: A review of recent developments. *Nanotechnology* **2019**, *30*, 312001. [CrossRef] [PubMed]
22. Acharya, V.; Agarwal, K.; Mondal, S. Electronic materials for solution-processed tfts. *Mater. Res. Express* **2023**, *10*, 082002. [CrossRef]
23. Jo, J.-W.; Kang, S.-H.; Heo, J.S.; Kim, Y.-H.; Park, S.K. Flexible metal oxide semiconductor devices made by solution methods. *Chem. Eur. J.* **2020**, *26*, 9126–9156. [CrossRef]
24. Kim, D.J.; Kim, D.L.; Rim, Y.S.; Kim, C.H.; Jeong, W.H.; Lim, H.S.; Kim, H.J. Improved electrical performance of an oxide thin-film transistor having multistacked active layers using a solution process. *ACS Appl. Mater. Interfaces* **2012**, *4*, 4001–4005. [CrossRef]
25. Hwang, Y.-J.; Kim, D.-K.; Jeon, S.-H.; Wang, Z.; Park, J.; Lee, S.-H.; Jang, J.; Kang, I.M.; Bae, J.-H. Importance of structural relaxation on the electrical characteristics and bias stability of solution-processed ZnSno thin-film transistors. *Nanomaterials* **2022**, *12*, 3097. [CrossRef]
26. Kim, Y.-H.; Heo, J.-S.; Kim, T.-H.; Park, S.; Yoon, M.-H.; Kim, J.; Oh, M.S.; Yi, G.-R.; Noh, Y.-Y.; Park, S.K. Flexible metal-oxide devices made by room-temperature photochemical activation of sol–gel films. *Nature* **2012**, *489*, 128–132. [CrossRef]
27. Zhao, Y.; Wang, Z.; Xu, G.; Cai, L.; Han, T.-H.; Zhang, A.; Wu, Q.; Wang, R.; Huang, T.; Cheng, P.; et al. High-performance indium-gallium-zinc oxide thin film transistor via interface engineering. *Adv. Funct. Mater.* **2020**, *30*, 2003285. [CrossRef]
28. Kim, D.-K.; Seo, K.-H.; Kwon, D.-H.; Jeon, S.-H.; Hwang, Y.-J.; Wang, Z.; Park, J.; Lee, S.-H.; Jang, J.; Kang, I.M.; et al. Viable strategy to minimize trap states of patterned oxide thin films for both exceptional electrical performance and uniformity in sol–gel processed transistors. *Chem. Eng. J.* **2022**, *441*, 135833. [CrossRef]
29. Tsay, C.-Y.; Yan, T.-Y. Solution processed amorphous InGaZnO semiconductor thin films and transistors. *J. Phys. Chem. Solids.* **2014**, *75*, 142–147. [CrossRef]
30. Rim, Y.S.; Jeong, W.H.; Kim, D.L.; Lim, H.S.; Kim, K.M.; Kim, H.J. Simultaneous modification of pyrolysis and densification for low-temperature solution-processed flexible oxide thin-film transistors. *J. Mater. Chem.* **2012**, *22*, 12491–12497. [CrossRef]
31. Oh, C.; Jung, H.; Park, S.H.; Kim, B.S. Enhanced electrical properties of In-Ga-Sn-O thin films at low-temperature annealing. *Ceram. Int.* **2022**, *48*, 9817–9823. [CrossRef]
32. Nomura, K.; Ohta, H.; Takagi, A.; Kamiya, T.; Hirano, M.; Hosono, H. Room-temperature fabrication of transparent flexible thin-film transistors using amorphous oxide semiconductors. *Nature* **2004**, *432*, 488–492. [CrossRef]
33. Parthiban, S.; Kwon, J.Y. Role of dopants as a carrier suppressor and strong oxygen binder in amorphous indium-oxide-based field effect transistor. *J. Mater. Res.* **2014**, *29*, 1585–1596. [CrossRef]
34. Park, S.; Kim, K.-H.; Jo, J.-W.; Sung, S.; Kim, K.-T.; Lee, W.-J.; Kim, J.; Kim, H.J.; Yi, G.-R.; Kim, Y.-H.; et al. In-depth studies on rapid photochemical activation of various sol–gel metal oxide films for flexible transparent electronics. *Adv. Funct. Mater.* **2015**, *25*, 2807–2815. [CrossRef]
35. Isik, M.; Gasanly, N. Composition-tuned band gap energy and refractive index in $GaSxSe_{1-x}$ layered mixed crystals. *Mater. Chem. Phys.* **2017**, *190*, 74–78. [CrossRef]
36. Tak, Y.J.; Ahn, B.D.; Park, S.P.; Kim, S.J.; Song, A.R.; Chung, K.-B.; Kim, H.J. Activation of sputter-processed indium–gallium–zinc oxide films by simultaneous ultraviolet and thermal treatments. *Sci. Rep.* **2016**, *6*, 21869. [CrossRef]

37. Kwon, S.; Hong, J.; Jun, B.-H.; Chung, K.-B. Improvement of electrical performance by neutron irradiation treatment on IGZO thin film transistors. *Coatings* **2020**, *10*, 147. [CrossRef]
38. Lee, S.; Ghaffarzadeh, K.; Nathan, A.; Robertson, J.; Jeon, S.; Kim, C.; Song, I.-H.; Chung, U.-I. Oxi Trap-limited and percolation conduction mechanisms in amorphous oxide semiconductor thin film transistors. *Appl. Phys. Lett.* **2011**, *98*, 203508. [CrossRef]
39. Lee, S.; Nathan, A. Localized tail state distribution in amorphous oxide transistors deduced from low temperature measurements. *Appl. Phys. Lett.* **2012**, *101*, 113502. [CrossRef]
40. Faber, H.; Das, S.; Lin, Y.-H.; Pliatsikas, N.; Zhao, K.; Kehagias, T.; Dimitrakopulos, G.; Amassian, A.; Patsalas, P.A.; Anthopoulos, T.D. Heterojunction oxide thin-film transistors with unprecedented electron mobility grown from solution. *Sci. Adv.* **2017**, *3*, e1602640. [CrossRef]
41. Lee, S.; Jeon, S.; Nathan, A. Modeling Sub-Threshold Current–Voltage Characteristics in Thin Film Transistors. *J. Disp. Technol.* **2013**, *9*, 883–889.
42. Kim, D.-H.; Jeong, H.-S.; Lee, D.-H.; Bae, K.-H.; Lee, S.; Kim, M.-H. Quantitative analysis of positive-bias-stress-induced electron trapping in the gate insulator in the self-aligned top gate coplanar indium–gallium–zinc oxide thin-film transistors. *Coatings* **2021**, *24*, 1192. [CrossRef]
43. Kim, D.H.; Choi, S.; Jang, J.; Kang, H.; Kim, D.M.; Choi, S.-J.; Kim, Y.-S.; Oh, S.; Baeck, J.H.; Bae, J.U.; et al. Experimental decomposition of the positive bias temperature stress-induced instability in self-aligned coplanar InGaZnO thin-film transistors and its modeling based on the multiple stretched-exponential functions. *J. Soc. Inf. Disp.* **2017**, *25*, 98–107. [CrossRef]
44. Lee, J.-M.; Cho, I.-T.; Lee, J.-H.; Kwon, H.-I. Bias-stress-induced stretched-exponential time dependence of threshold voltage shift in InGaZnO thin film transistors. *Appl. Phys. Lett.* **2008**, *93*, 093504. [CrossRef]
45. Xu, P.-R.; Yao, R.-H. Threshold-voltage shift model based on electron tunneling under positive gate bias stress for amorphous InGaZnO thin-film transistors. *Displays* **2018**, *53*, 14–17. [CrossRef]
46. Wang, L.L.; Liu, T.C.; Cai, Y.; Zhang, S. Thin-film transistor Vth shift model based on kinetics of electron transfer in gate dielectric. *IEEE Trans. Electron Devices* **2014**, *61*, 1436–1443. [CrossRef]